applied sciences

MDPI

Article

Investigation of Wear and Friction Behavior of Cobalt-Chromium-Molybdenum Alloy Produced by Laser Powder Bed Fusion

Maziar Ramezani [1,*] and Zaidi Mohd Ripin [2]

[1] Department of Mechanical Engineering, Auckland University of Technology, Auckland 1010, New Zealand
[2] School of Mechanical Engineering, Universiti Sains Malaysia, Nibong Tebal 14300, Malaysia; mezaidi@usm.my
* Correspondence: maziar.ramezani@aut.ac.nz

Abstract: This study investigates the sliding wear resistance of the Co-28Cr-6Mo alloy manufactured by laser-based powder bed fusion through linear reciprocating sliding wear tests. Varied loads and sliding speeds, in both dry and lubricated contact scenarios, were examined using a hardened steel ball as a counter material. Microhardness profiles were obtained to understand the alloy's mechanical behavior, revealing consistent average microhardness values of 409.67 HV through the thickness and 404.05 HV along the wear track. The coefficient of friction (COF) indicated a decrease in COF with an increase in the applied normal load in both dry and lubricated contacts. On the other hand, the COF increased with higher sliding speeds, and remained stable under lubricated contact but fluctuated in dry conditions over time. Increased applied load and sliding speed correlated with escalated wear rates. Investigation of the impact of different lubricants on tribological properties highlighted synthetic gear oil as the most effective in reducing wear rate among tested lubricants. Wear mechanisms were elucidated through scanning electron microscopy and energy-dispersive X-ray spectroscopy. The presented results can serve as a guide for selecting suitable operating conditions and lubricants to reduce wear in Co-Cr-Mo alloy applications.

Keywords: cobalt-chromium-molybdenum; Co-Cr-Mo alloy; selective laser melting; sliding wear; tribology

Citation: Ramezani, M.; Ripin, Z.M. Investigation of Wear and Friction Behavior of Cobalt-Chromium-Molybdenum Alloy Produced by Laser Powder Bed Fusion. *Appl. Sci.* **2023**, *13*, 10582. https://doi.org/10.3390/app131910582

Academic Editor: Antonio Miotello

Received: 31 July 2023
Revised: 12 September 2023
Accepted: 15 September 2023
Published: 22 September 2023

1. Introduction

Powder bed fusion (PBF) is a type of additive manufacturing (AM) that involves the use of a laser or electron beam to melt and fuse layers of powdered material together to create a three-dimensional object [1,2]. In PBF, a layer of powder is spread across a built platform, and the laser or electron beam selectively melts and fuses the powder together according to a digital model of the object being printed. Once the first layer is complete, another layer of powder is spread on top, and the process is repeated until the object is fully printed [3–5].

There are several types of PBF processes, including selective laser sintering (SLS), selective laser melting (SLM), and electron beam melting (EBM). These processes differ in the type of energy source used to melt the powder and the way in which the powder is delivered to the build platform [6,7]. Laser-based powder bed fusion of metals (PBF-LB/M) uses a high-powered laser beam to melt and fuse powdered materials, typically metal alloys. A thin layer of powder is spread over a build platform and selectively melted by the laser beam according to a 3D computer-aided design model. The build platform is then lowered by a distance equal to the layer thickness, and the process is repeated with the next layer of powder. This process is repeated layer by layer until the object is complete.

One of the key advantages of PBF-LB/M is its ability to produce complex geometries with high precision and accuracy. This is due to the high resolution of the laser beam, which can be focused to a spot size of a few tens of microns, allowing for the creation of intricate

details and fine features. Additionally, the PBF-LB/M process can produce objects with a high density, as the melted powder is rapidly cooled and solidified, resulting in a strong and dense final product [8,9].

Cobalt-chromium-molybdenum (Co-Cr-Mo) is one of the alloys used in the PBF-LB/M process. The Co-Cr-Mo alloy is a well-known biomaterial used in medical applications due to its excellent mechanical properties, including high strength, good fatigue resistance, biocompatibility, and corrosion resistance. The PBF-LB/M of the Co-Cr-Mo alloy has been shown to have great potential for intricate and precise fabrication of complex shapes, which is particularly advantageous for producing personalized and patient-specific biomedical implants like joint replacements and dental implants. The PBF-LB/M Co-Cr-Mo alloy is also used in aerospace, automotive, tooling and machinery applications [10]. For example, it can be used to manufacture intricate turbine blades and engine components, or it can also be utilized in cutting tools to benefit from the alloy's high hardness and resistance to abrasion, allowing for extended tool life and improved efficiency.

Although several papers have been published on the microstructure and mechanical properties of cobalt-chromium alloys manufactured by PBF additive manufacturing [11–15], the study of the tribological performance of the alloy is rare. Schwindling et al. [16] studied the wear resistance of the Co-Cr alloy manufactured by SLM for dental applications. They used a biaxial chewing simulator for the wear tests at a constant load, with alumina ceramic as the counter material and deionized water as the lubricant. Their results suggest that SLM-CoCr is highly wear-resistant and could be an alternative for manufacturing prosthetic restorations, even in areas with occlusal loading. However, the effect of different working conditions and the morphology of the wear track of the alloy have not been studied. In another study, Duran et al. [17] investigated the tribological performance of Co-Cr-Mo alloys fabricated by casting and SLM under dry and wet conditions. The tribological properties were evaluated using a reciprocating wear tester, with artificial saliva solution used for the lubricated tests at room temperature. The results indicated that the SLM-processed alloy showed superior wear performance under dry sliding conditions, but experienced more wear under wet conditions. However, no in-depth analysis of the wear mechanisms of the alloy in dry and lubricated conditions was conducted, and the effects of varying loads and speeds on the friction and wear behavior of the alloy have not been investigated.

Fu et al. [18] investigated the wear resistance and biocompatibility of Co-Cr dental alloys, produced using the casting and SLM methods. The aim of their study was to compare the suitability of SLM versus traditional casting for producing dental Co-Cr alloys. The microstructure, surface composition, mechanical properties, and wear resistance of the alloys were evaluated. The authors conducted the sliding wear tests using a ball-on-disk tribometer with a silicon nitride ceramic ball as the counter material. Their results showed that SLM alloys exhibited shallower wear scars and less wear debris compared to the cast alloys. However, they only applied a constant load of 5N at a constant rotational speed and did not investigate the effects of load and sliding speed on the coefficient of friction and wear rate. They also did not investigated the wear mechanisms of the alloy, and the duration of their tests was only 30 min. Another limitation of their study was that it was only conducted in dry contact, and the effect of lubrication was not investigated.

Tonelli et al. [19] analyzed the effect of post-process heat treatment on the hardness, microstructure, and sliding wear behavior of Co-28Cr-6Mo alloy manufactured by SLM. The dry sliding wear behavior of the as-built and heat-treated Laser-PBF Co-28Cr-6Mo alloy was studied, with the conventional wrought alloy used as a benchmark. An AISI 52100 steel cylinder was used as the counter surface, and it was observed that the as-built LPBF alloy displayed greater wear resistance than the conventional wrought alloy. The optimized aging treatment significantly altered the as-built Laser-PBF microstructure, improved the alloy's hardness, and generally improved its friction and wear behavior. However, the sliding wear tests were only conducted in dry contact, with no variations in the sliding speed.

As can be seen from the above literature review, a systematic study has not been conducted yet to investigate the tribological performance of the PBF-LB/M Co-Cr-Mo alloy under different working conditions, and the wear morphology and mechanisms have not been explored in detail. Therefore, in this paper, we are presenting the results of sliding wear tests of the PBF-LB/M Co-28Cr-6Mo alloy under a range of applied loads, sliding speeds, and lubricants. The friction and wear behavior of the Co-28Cr-6Mo alloy is compared with the samples produced by the traditional casting process. In order to investigate the wear mechanisms and chemical compositions of the wear tracks, we employed scanning electron microscopy (SEM) and Energy-dispersive X-ray spectroscopy (EDX). The findings obtained from this study can be utilized as a resource for selecting suitable operating conditions to minimize wear in PBF-LB/M Co-28Cr-6Mo alloy applications.

2. Materials and Methods

The specimens were produced using an industrial 3D printer manufactured by Renishaw (Wotton-under-Edge, UK). The printer model, Ren AM 250 SLM, was used with an upgraded laser system that can deliver a maximum laser power of 400 W. The SLM machine has a build volume of 250 mm × 250 mm × 300 mm (Z-axis), and the default laser spot size diameter is θ = 140 µm. To maintain optimal printing conditions, the oxygen concentration inside the building chamber was controlled to be below 50 ppm. According to the manufacturer's recommendations, the ideal powder for the printer should be spherical in shape and have a particle size range of 15 µm to 45 µm.

The Co-Cr-Mo specimens with the dimensions of 40 mm × 20 mm × 10 mm were fabricated using a metal powder that complies with the Co-Cr-Mo ASTM F75 standard [20], which was provided by Renishaw. The powder had a composition in wt% of 64.15 Co, 28.81 Cr, 5.21 Mo, and small amounts of other elements including Ni, Fe, C, Si, Mg, W, P, S, Al, Ti, and Co (balance). Molybdenum enhances strength and heat resistance, while chromium provides resistance to oxidation and corrosion. Table 1 presents the SLM process parameters used to produce the Co-Cr-Mo samples. The values presented in the table represent the optimal process parameters as recommended by the SLM machine manufacturer for the Co-Cr-Mo powder. These parameters are designed to achieve the best balance of mechanical strength, hardness, and density, while also minimizing the occurrence of the lack of fusion during the printing process. The temperature during the SLM printing was set at 1350° to ensure the melting and proper fusion of the Co-Cr-Mo alloy powder layers during the SLM process.

Table 1. Optimum process parameters for powder bed fusion selective laser melting of cobalt-chromium-molybdenum alloy.

Parameters	Value
Laser powers	320 W
Layer thickness	0.04 mm
Scanning strategy	Parallel scanning 67° rotation after each layer
Scan speeds	700 mm/s
Hatch distance	0.09 mm

For polishing, manual rotary grinding–polishing was initially used with silicon carbide papers of 180, 500, 1200, and 2400 grit. Subsequently, the Struers TegraPol-25 automatic polishing machine with TegraForce-5 for rotation and TegraDoser-5 for liquid dispensing refined the process. Successive 3 µm grit diamond polishing ("DiaPro") and 1 µm grit colloidal silica polishing ("OP-S Suspension") steps were used for a mirror-like finish. Samples were etched with a 10% H_2SO_4 and CH_3OH solution for 25 s at room temperature. Polished samples were subjected to hardness tests using a Leco LM-800AT microhardness

tester with a load of 1 kgf. The density of the samples was determined using the Archimedes' principle method. This involved measuring both the mass and volume of the samples and then calculating the density by dividing the mass by the volume.

Sliding wear experiments were conducted using a Ducom Instruments TR-282 linear reciprocating tribometer. A range of normal loads (5 N, 10 N, 15 N), and sliding frequencies (2 Hz, 5 Hz, 8 Hz) were used for the sliding wear tests. The tests were conducted in both dry and lubricated conditions, with a 10 mm diameter hardened steel ball, with a roughness of Ra = 1.2 μm as the counter material. Different types of lubricants (gear oil, paraffin oil, castor oil, ester oil, and deionized water) were used for the lubricated sliding wear tests. These lubricants were selected to cover a broad range of kinematic viscosities. By including lubricants with varying viscosities, we aimed to investigate how different lubrication conditions influence the tribological behavior of the system. The tribometer was set for a wear track (sliding stroke) of 10 mm, and a total sliding distance of 1000 m was used for all tests. All tests were conducted at room temperature (22 °C). Each test set was repeated at least three times, and the average values of the COF and wear rates are reported in this paper.

To measure the cross-sectional area of the wear tracks, a Taylor Hobson Form Talysurf 50 stylus profilometer was used. Five sections of each wear track were scanned by the stylus profilometer to obtain a raw profile graph of the worn surface of the sample, which determined the depth and width of the wear scars. The average wear scar surfaces were calculated using Image J 1.5.3, an image analysis software, and the average cross-sectional area was multiplied by the wear track length (10 mm) to obtain the wear volume. Wear rates (mm^3/m) were then calculated by dividing the average wear volume (mm^3) by the sliding wear distance (m).

To observe the microstructure and wear mechanisms, the tested samples were examined under a Hitachi SU-70 field emission scanning electron microscope (FE-SEM). Energy-dispersive X-ray spectroscopy (EDX) was also used to identify and quantify the elemental composition of the worn surfaces.

3. Results and Discussions

The morphology of the powder used for PBF-LB/M printing is shown in Figure 1a. The powder has a particle size range of 15 μm to 45 μm. Figure 1b shows the microstructure of the PBF-LB/M Co-Cr-Mo alloy. During PBF-LB/M, the laser melts the powder and creates a melt pool, which is the region of molten metal that solidifies to form the final part. The melt pool boundaries are the regions where the molten metal transitions to the solid phase. These boundaries can be observed in Figure 1b. One common defect in PBF-LB/M parts is lack of fusion (LoF), which occurs when the laser fails to completely melt and fuse adjacent layers of powder particles together. LoF can occur due to insufficient laser power, slow scanning speed, or insufficient powder bed preheating. When LoF occurs, the unmelted or partially melted powder particles can create voids or cracks in the final part, reducing its strength and integrity [21,22]. In this research, the optimum PBF-LB/M process parameters recommended by Renishaw were used for printing the samples; however, regions with LoF and pores can still be observed in the samples.

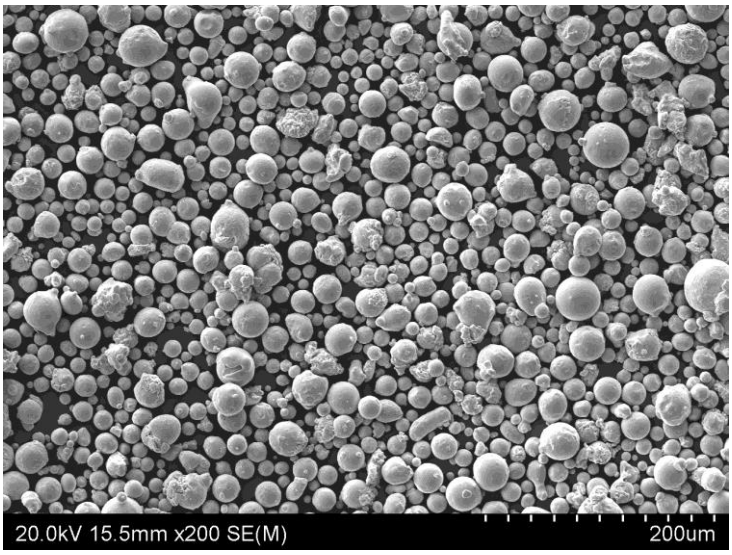

(**a**)

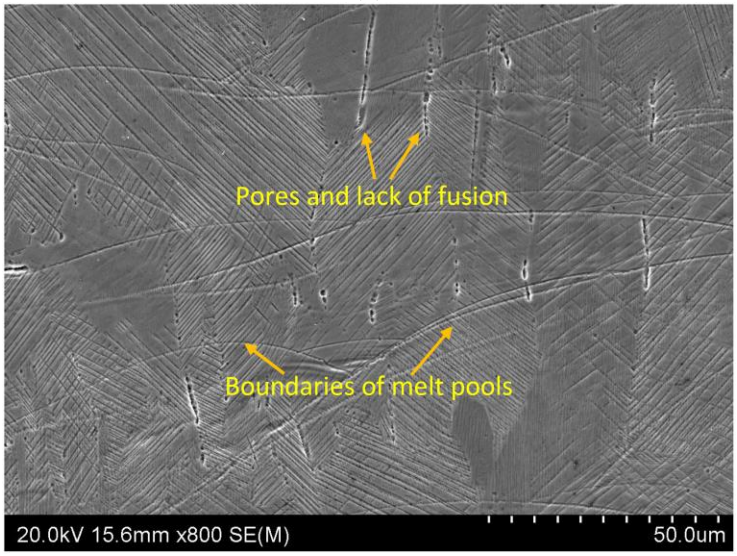

(**b**)

Figure 1. (**a**) Morphology of the Co-Cr-Mo powder, (**b**) Melt pool boundaries and lack of fusion of as-printed Co-Cr-Mo alloy samples.

The SLM-printed samples had an average surface roughness (Ra) of 7.3578 ± 0.1384 µm and a density of 8125 ± 36.22 kg/m^3. They had an average yield strength of 693 ± 12 MPa and an ultimate tensile strength of 1096 ± 15 MPa with elongation at break of 18% ± 2%. Figure 2 shows the microhardness profiles of printed samples along the wear track and through the thickness. These data can be used to investigate changes in the mechanical properties of the material due to variations in the processing parameters or thermal history. The results show a quite uniform hardness profile with an average microhardness of 409.67 HV through the thickness and 404.05 HV along the wear track.

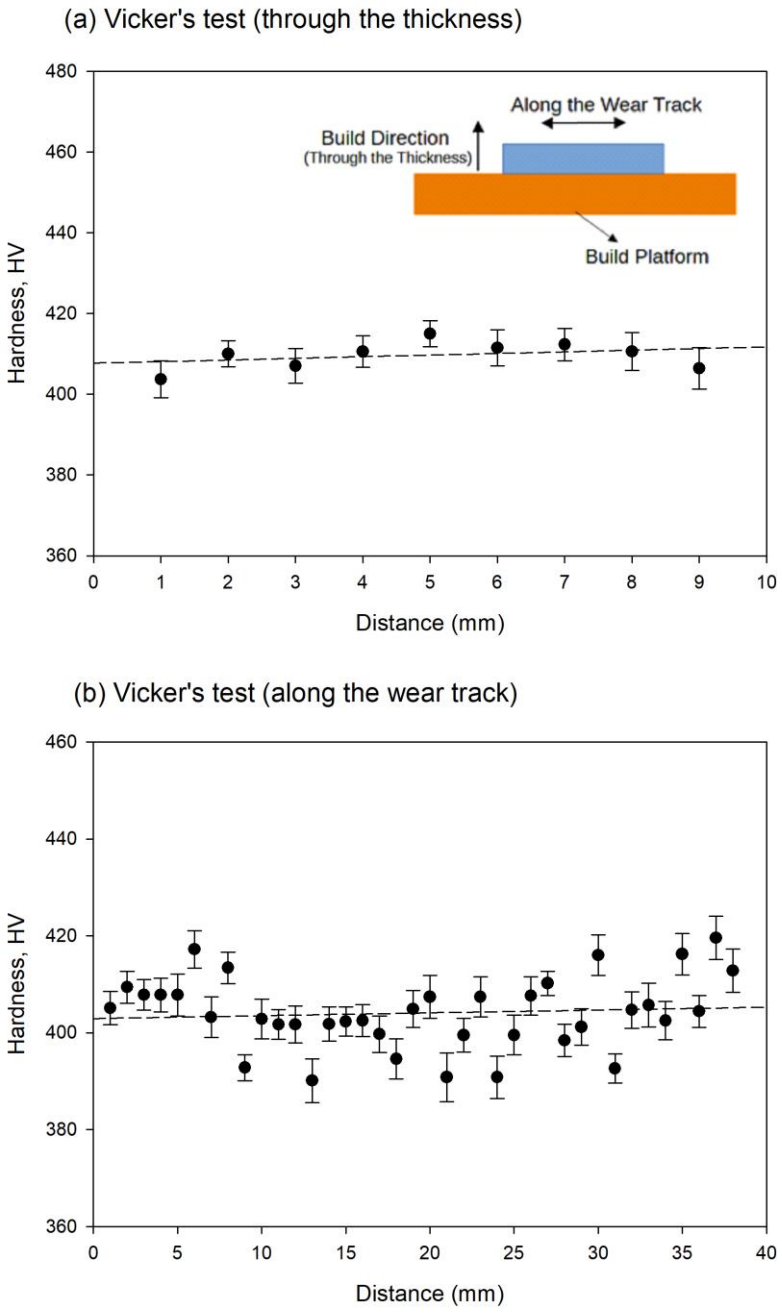

Figure 2. Hardness profiles of as-printed samples (**a**) through the thickness, and (**b**) along the wear track.

It is worth pointing out that the build direction of the samples was through the thickness in this research. The reason for the slightly higher hardness through the thickness of the SLM-printed samples could be the fact that the heat transfer during the PBF-LB/M process is different in the build direction compared to the other directions. In the PBF-LB/M process, heat is primarily applied to the top surface of the powder bed through the laser beam. This concentrated heat source melts and fuses the powder, causing the material to solidify as the heat dissipates from the top layers downward. Consequently, the cooling rate in the build direction may vary, potentially affecting the microstructure, including grain size. In some cases, a slower cooling rate can lead to the formation of larger grains, which can have implications for material properties. Larger grain sizes are often associated with changes in microhardness values, although the exact relationship can depend on various factors, including material composition and processing parameters. Additionally,

the residual stresses within the material can be different in the build direction compared to the other directions, which can also affect the microhardness [23,24].

Figure 3 shows the average coefficient of friction (COF) for SLM-printed samples tested under different loads and sliding frequencies. Mobil Gear SHC 150 (Synthetic gear oil) was used for the lubricated test results presented in Figure 3. It can be observed that in both dry and lubricated contacts, as the applied normal load increases, COF decreases. At higher loads, there is an increase in the contact area between the two surfaces in contact, which can lead to a decrease in the localized pressure and shear stresses in the contact area. This can result in a decrease in the frictional resistance between the two surfaces, as the deformation and adhesion at the interface are reduced [25].

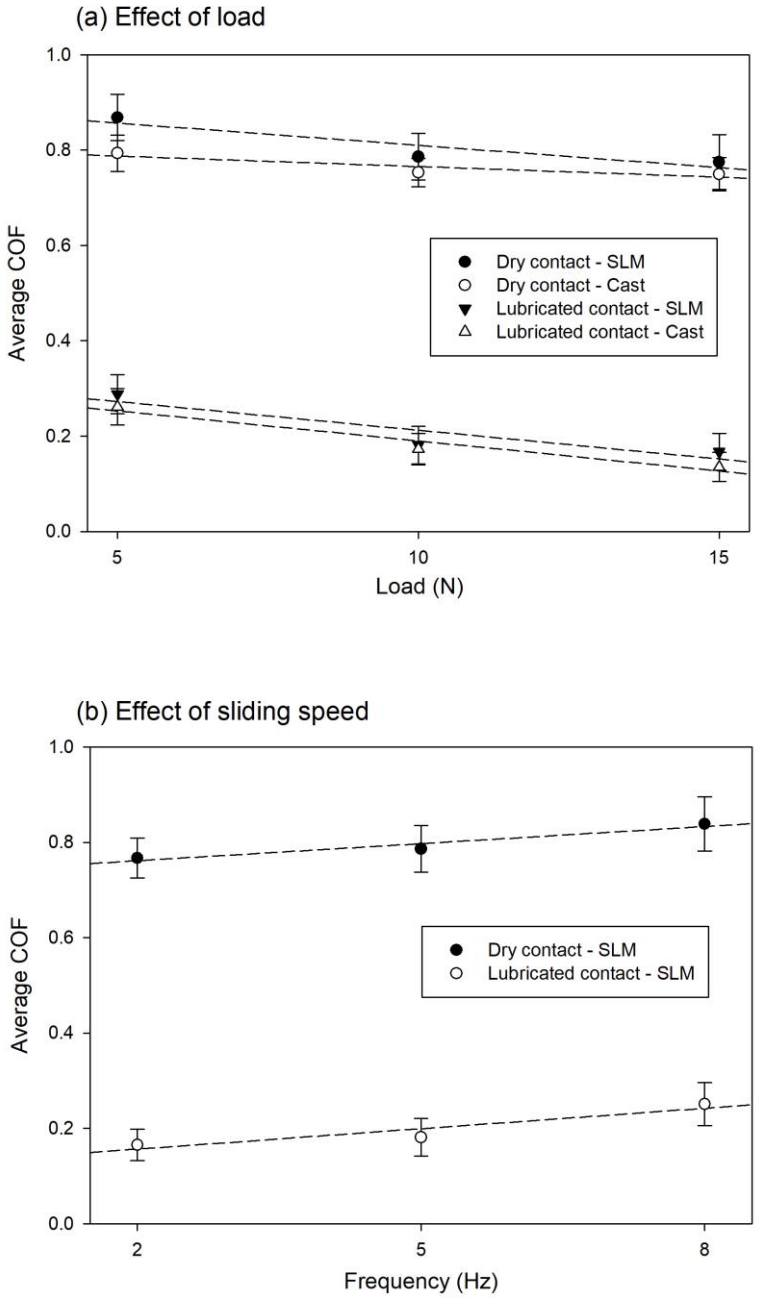

Figure 3. Effects of (**a**) applied normal load (at 5 Hz frequency), and (**b**) frequency (at 10 N constant load), on average coefficient of friction. All lubricated tests were conducted using synthetic gear oil.

However, at higher sliding speeds, COF increases. This is because of the increase in interface temperature due to frictional heating at higher sliding speeds. This can cause

thermal softening of the material and the formation of adhesion between the two surfaces, leading to an increase in friction coefficient. Also in lubricated contact, higher sliding speeds lead to a reduction in the time available for the lubricant to form a complete film between the two sliding surfaces. As a result, the surfaces come in contact with each other, leading to higher friction.

The variation of COF with test time can be observed in Figure 4. In dry contact, the COF starts high at around 0.8 and maintains this average value during the test. The COF graph for dry contact shows fluctuations and instability in the friction coefficient due to the lack of lubrication. In dry contact, the surfaces can experience adhesion, plowing, and/or deformation, which can lead to high friction and wear. The asperities on the surfaces may interlock, leading to a higher friction coefficient during initial contact [26]. As the surfaces continue to slide, the asperities may break off or wear down, leading to a reduction in friction coefficient. However, as the surface roughness continues to change over time due to wear and other factors, the friction coefficient may also experience fluctuations. This can result in a rough friction coefficient graph with many peaks and valleys over time. On the other hand, COF during the lubricated sliding wear test is significantly lower, showing the effectiveness of lubrication for the Co-Cr-Mo alloy. The results showed that the lubricant film did not break down or become depleted during the test and a low value of COF was maintained.

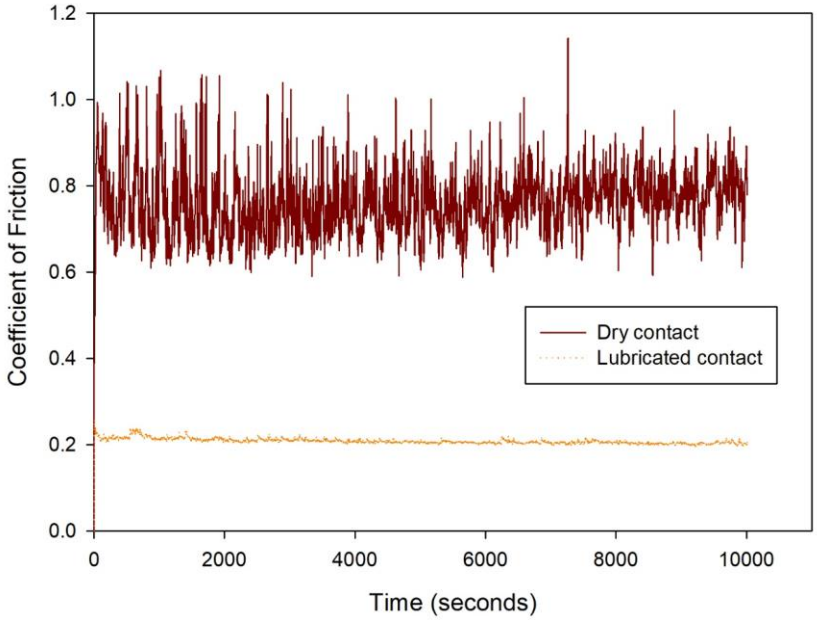

Figure 4. Variation of coefficient of friction with test time for SLM samples tested at room temperature, under a 10 N load, and a 5 Hz frequency. The lubricated test was conducted using synthetic gear oil.

Figure 5 shows the effects of load and sliding speed on the wear rate of an SLM-printed Co-Cr-Mo alloy. As expected, the wear rate in lubricated contact is significantly lower than in dry contact. As the applied load increases, the wear rate increases. The higher load results in higher contact pressure, and this increased pressure causes higher frictional forces between the surfaces, which can accelerate the wear rate. When a material is subjected to higher contact stress, it undergoes greater deformation, causing microcracks to form, leading to fatigue and eventual failure, which eventually increases the wear rate [27]. It can also be observed in Figure 5b that the wear rate increases at higher sliding speeds, although the effect of sliding speed is not as remarkable as the effect of applied load on the wear rate. Higher sliding speeds can generate more heat due to increased friction between the surfaces in contact. This increased heat causes softening of the material, which can increase the wear rate [28].

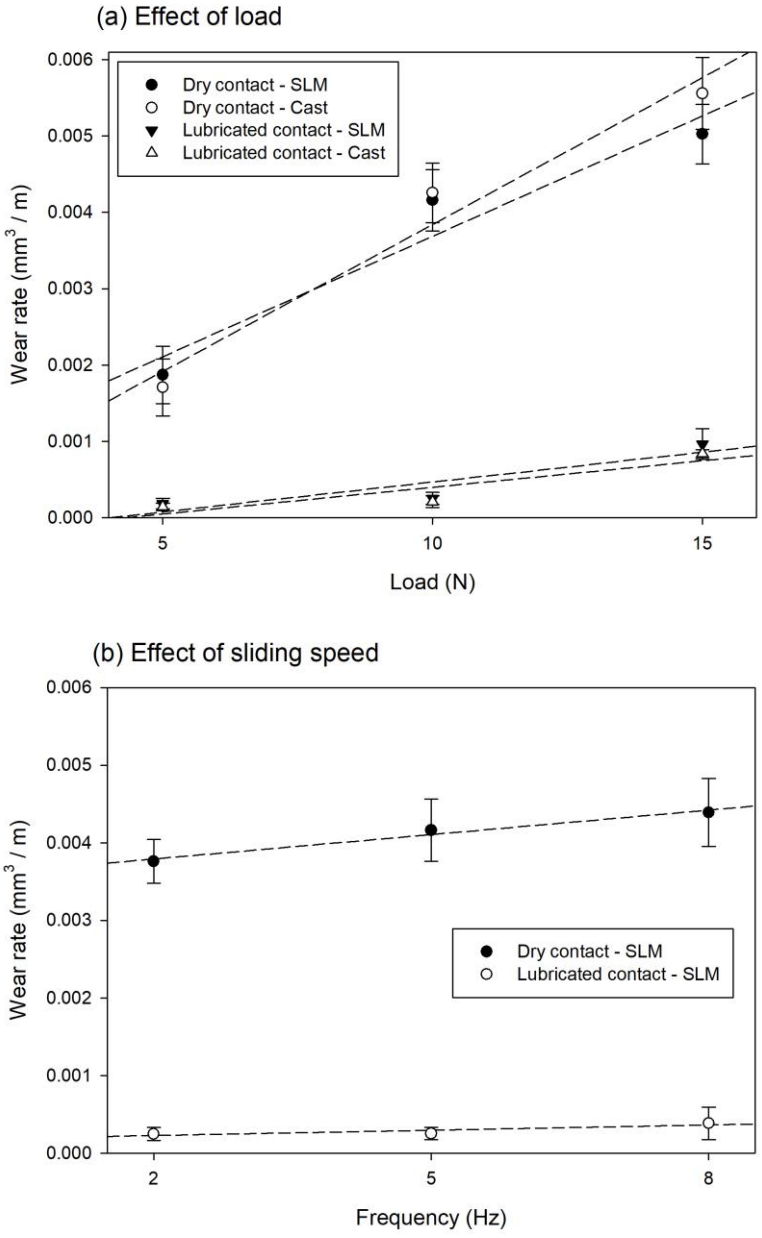

Figure 5. Effects of (**a**) applied normal load (at a 5 Hz frequency), and (**b**) frequency (at a 10 N constant load), on the wear rate. All lubricated tests were conducted using synthetic gear oil.

Figure 6 shows the effect of different types of lubricants on the tribological properties of an SLM-printed Co-Cr-Mo alloy. As can be seen in the figure, synthetic gear oil (MOBILGEAR SHC 150) with a kinematic viscosity at 40 °C of 150 cSt provides the best protection against wear, followed by polyphenyl ester oil (4P-3E) with a kinematic viscosity at 40 °C of 69.45 cSt, paraffin mineral oil with a kinematic viscosity at 40 °C of 18.73 cSt, and castor oil with a kinematic viscosity at 40 °C of 13.52 cSt. On the other hand, using deionized water as a lubricant for the Co-Cr-Mo alloy leads to the highest wear rate.

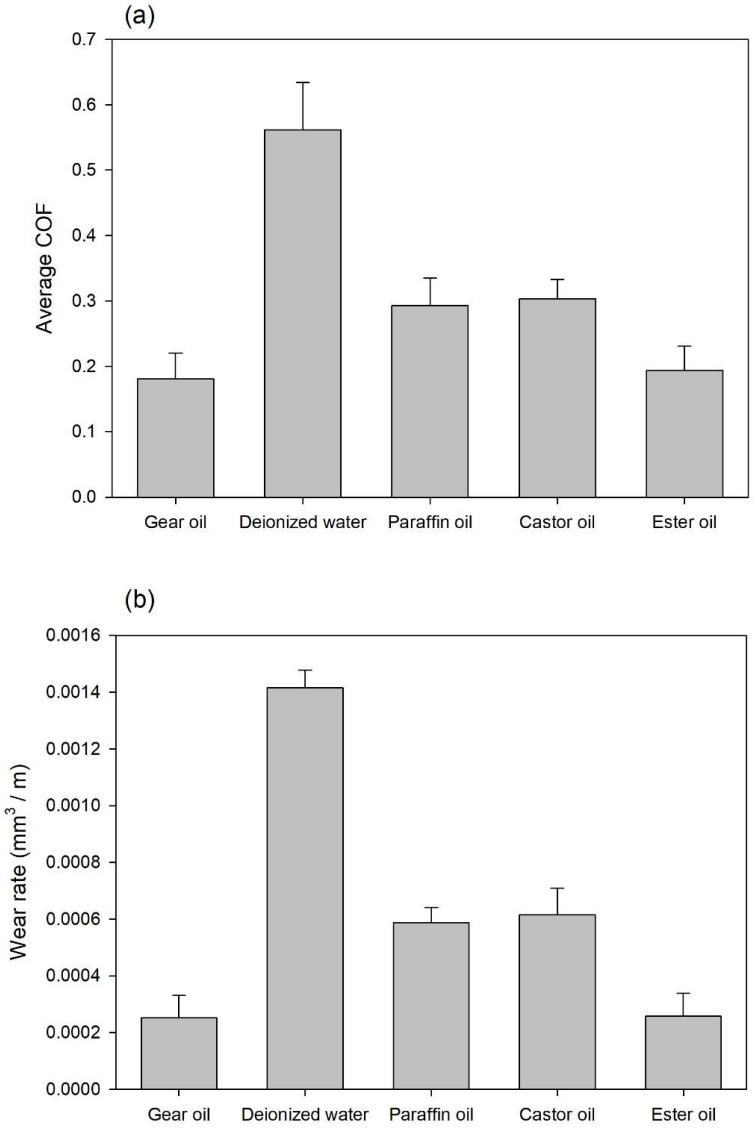

Figure 6. Effects of different types of lubricants on (**a**) average coefficient of friction, and (**b**) wear rate of SLM samples. All tests were conducted at room temperature under a 10 N load and a 5 Hz frequency.

An SEM image of the whole wear track of a sample tested in the dry condition is shown in Figure 7. Relatively smooth edges with noticeable longitudinal grooves can be seen in the SEM image, with some wear debris accumulated at the two ends of the wear track. With higher magnification SEM images in Figure 8, wear mechanisms can be identified. Figure 8a shows a wear track tested in dry contact. Grooves in the wear track show the main wear mechanism in dry contact is abrasive wear, where the hard particles (debris) slide against the test sample and plowed into the surface, causing material removal. The formation of cracks and the spalling (breaking off) of small particles or flakes from the surface occurs due to fatigue wear, where repeated cycles of stress can initiate and propagate surface cracks. Over time, the cracks can reach a critical size, causing small particles or flakes to break off from the surface. Galling can also be observed in Figure 8a, which is a type of wear mechanism that occurs when two metal surfaces in sliding contact undergo excessive friction and adhesion, resulting in localized welding and tearing of surface material. For lubricated contact, minimum wear loss can be observed in Figure 8b, with shallow grooves representing abrasive wear.

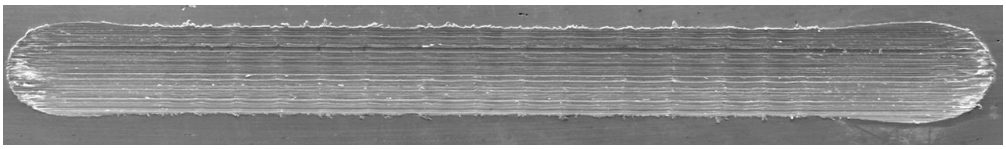

Figure 7. SEM image of the wear track of a sample tested under dry contact at a 5 Hz frequency, a 10 N load, and room temperature. Wear track length is 10 mm.

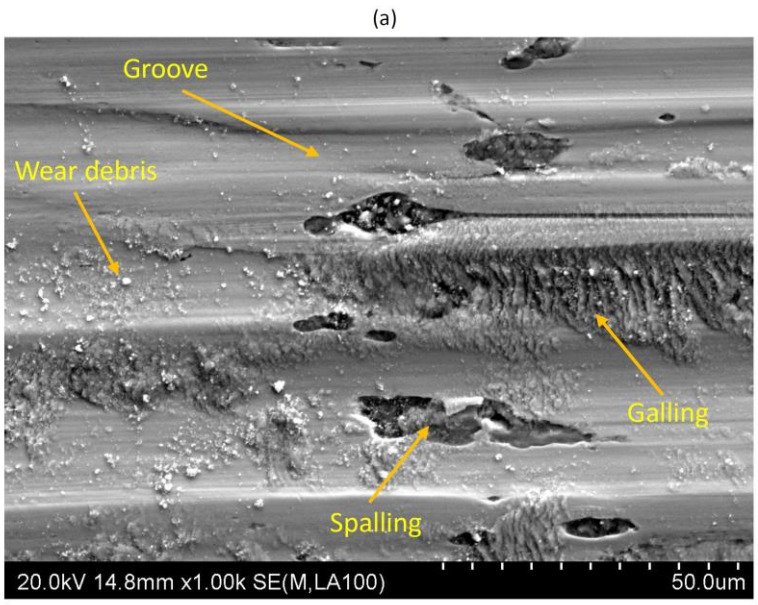

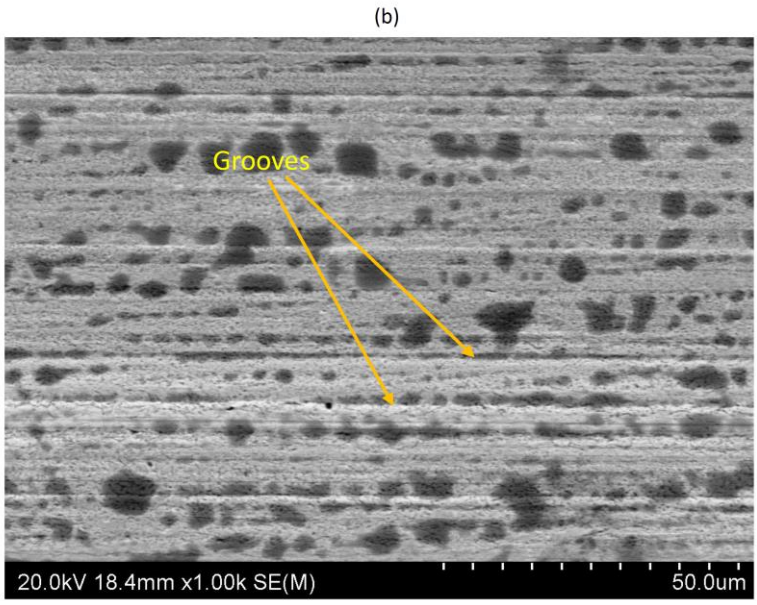

Figure 8. Wear tracks after reciprocating sliding wear tests under (**a**) dry contact; and (**b**) lubricated contact with gear oil. Both samples tested at 5 HZ and under a 10 N applied load and at room temperature.

To compare the COF and wear resistance of an SLM-printed Co-Cr-Mo alloy with a traditionally manufactured alloy, sliding wear tests were conducted on the Co-Cr-Mo alloy manufactured by the investment casting process. The comparison of the tribological performance of the two manufacturing processes can be observed in Figures 3a and 5a. The cast samples show a lower friction coefficient compared to SLM-printed samples at all three

tested loads. However, SLM-printed samples show better wear resistance, especially at higher loads. It was observed by SEM analysis that this is due to the entrapment of the wear debris inside the pores on the wear track. As can be seen in Figure 9a, the wear debris is entrapped inside pores on the wear track. As the test time increases (Figure 9b), more debris becomes embedded within the pores on the surface of the material and forms a protective layer against further wear. This mechanism leads to a lower wear rate in SLM-printed Co-Cr-Mo samples, although they show higher COF compared to cast samples.

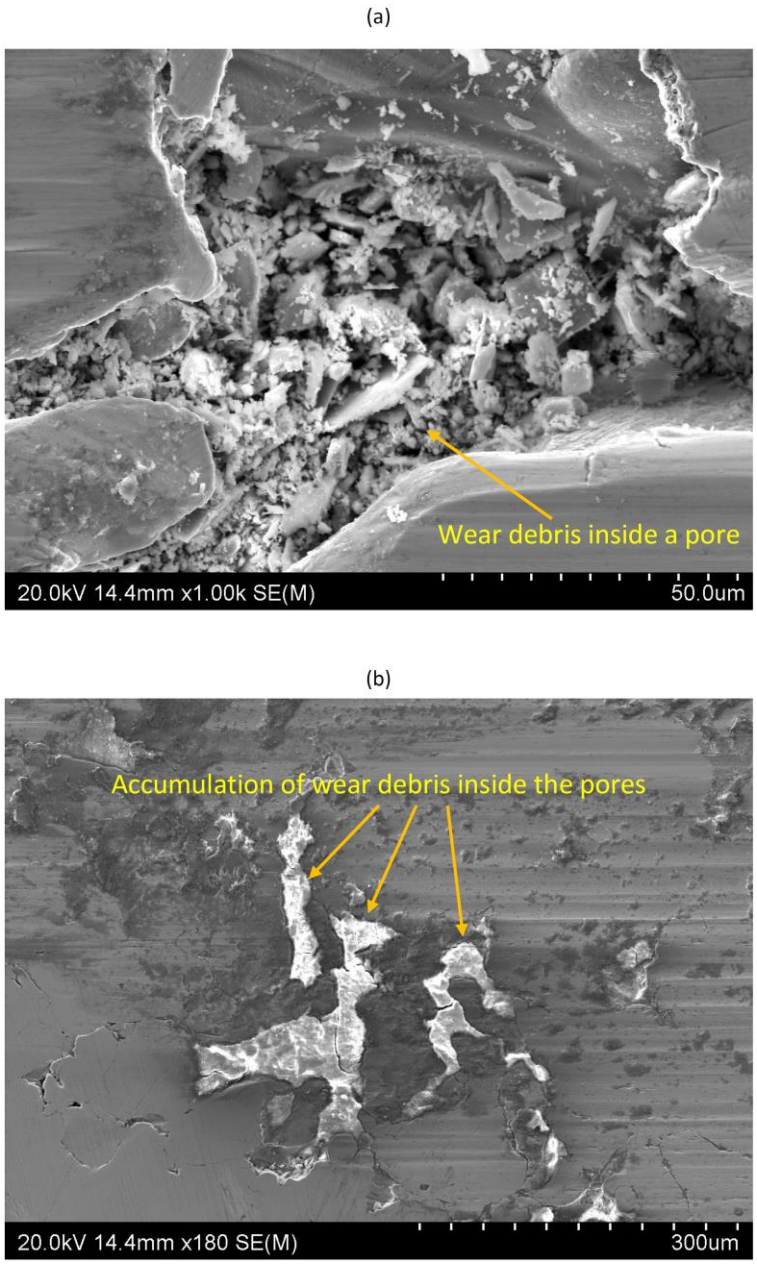

Figure 9. Accumulation of wear debris inside the pores on the wear track. Samples were tested at room temperature in dry contact under a 10 N load and a 5 Hz frequency. The test stopped after (**a**) 200 m, and (**b**) 600 m total sliding distance.

Figure 10 shows the cross-section of the wear track, for a sample tested at a 5 N load and a 5 Hz sliding frequency in dry contact. The subsurface cracks can be observed, representing fatigue wear due to cyclic loads applied to the surface of the samples during the reciprocating sliding wear test. The wear debris entrapped inside the surface pores can also be observed from the cross-section SEM image.

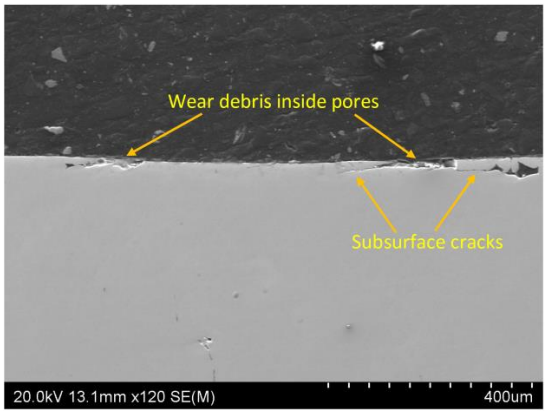

Figure 10. Subsurface of the wear track for a sample tested under a 5 N load and a 5 Hz frequency at room temperature and dry contact.

Figure 11 shows the EDX analysis of the wear track for a sample in dry contact under a 10 N load and a 5 Hz frequency. As expected, chromium (Cr), cobalt (Co), and molybdenum (Mo) are the primary elements present on the surface of the wear track. However, oxide particles can also be observed, with "pt1" having a composition of 5.86% oxygen (O). This is mainly because of the increase in the contact interface temperature (due to reciprocating sliding), leading to the oxidation of the wear debris and surface particles.

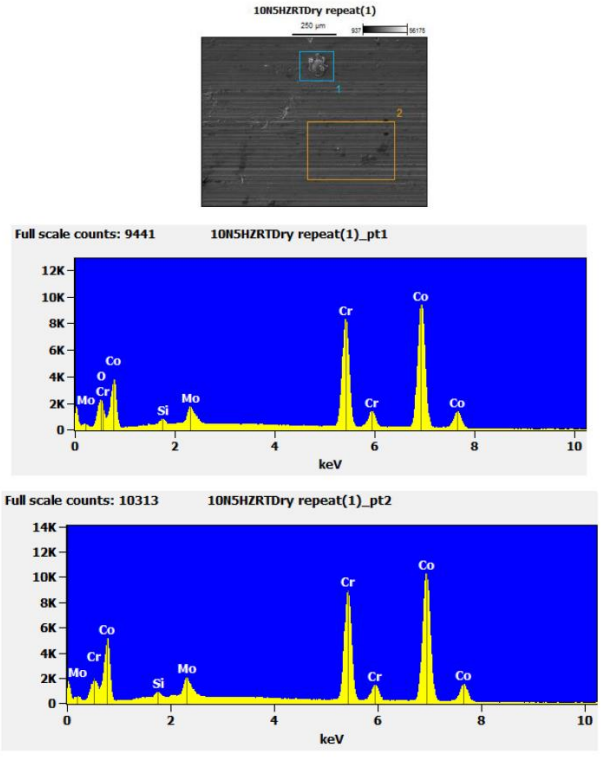

Weight %

	O	Si	Cr	Co	Mo
pt1	5.86	0.85	27.72	60.68	4.88
pt2		0.87	28.87	64.56	5.70

Figure 11. EDX analysis of the wear track of a sample tested at room temperature, under dry contact, 10 N load, and 5 Hz frequency.

In the presented EDX results illustrating the elemental composition within the wear track, it is crucial to acknowledge the accuracy and associated uncertainties of the data. EDX analysis provides valuable insights into the presence of chemical elements at a mi-

croscale, although the reported weight percentages and atomic ratios may exhibit apparent precision. These seemingly precise values may not always reflect the absolute accuracy of the measurements due to inherent sources of uncertainty in the technique. Factors such as variations in sample preparation, beam interaction effects, and calibration uncertainties contribute to the overall uncertainty in the reported results. Nonetheless, it is important to highlight that EDX remains a valuable tool for identifying the presence of chemical elements and characterizing compositional trends, offering valuable insights into material behavior within the wear track. While the data may not always be entirely accurate, they serves as a robust measure for elucidating the available chemical elements and their distributions in the analyzed specimen.

Figure 12 shows the worn surface of the hardened steel ball. The grooves on the worn area show the dominant wear mechanism was abrasive wear, due to the presence of wear debris in the contact interface. It should be noted that after the sliding wear tests, the wear volume of the ball was negligible, compared to the wear volume of the Co-Cr-Mo alloy. A small area at the edge of the worn surface was scanned and EDX spectra at each point were collected. The EDX mapping in Figure 12 shows the distribution of each element in the scanned area, with iron (Fe) being the primary element of the ball, with traces of Co and Cr wear debris being present on the ball's worn surface. Oxygen can also be observed, showing that the worn particles are being oxidated.

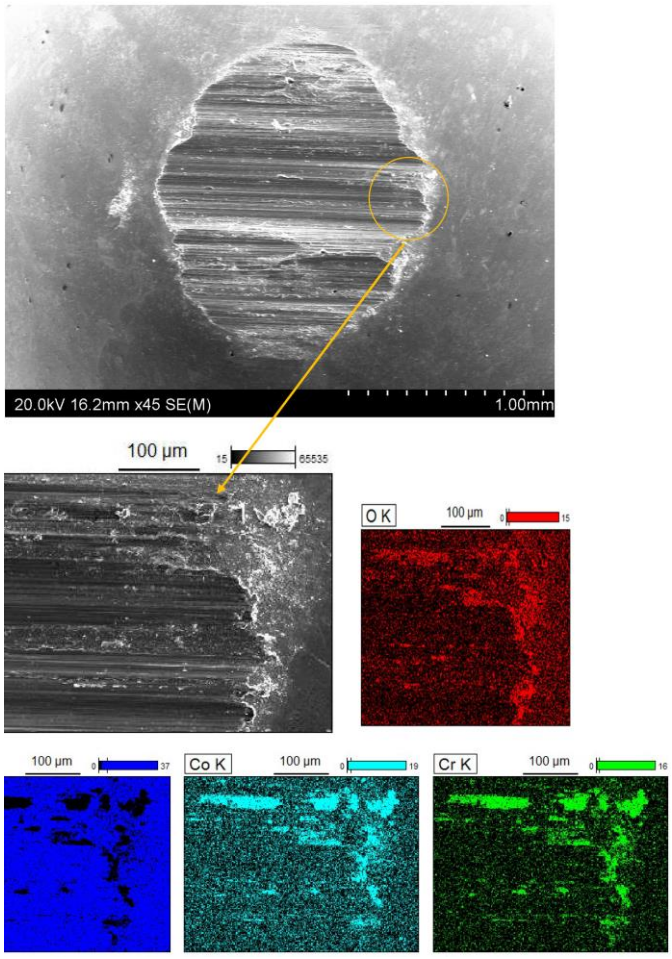

Figure 12. SEM image and EDX analysis of the hardened steel ball after sliding wear test at room temperature, under 5 Hz frequency, 10 N load, and dry contact). Cobalt-chromium alloy and oxygen can be observed on the ball surface.

4. Conclusions

This article discussed the results of a study on the tribological behavior of an SLM-printed Co-Cr-Mo alloy. The microstructure of the printed alloy showed the melt pool boundaries and lack of fusion defects. The microhardness profile reveals a uniform hardness with a slightly higher value through the thickness due to the difference in heat transfer and residual stresses within the material. The coefficient of friction (COF) was studied under different loads, sliding speeds, and lubricated conditions. In dry contact, the COF starts high and maintains the average high value during the test due to adhesion, plowing, and deformation. The main wear mechanism in dry contact was abrasive wear, with fatigue wear and adhesive wear also contributing to the overall material removal and wear rate of the material. In lubricated contact, the COF was significantly lower, showing the effectiveness of lubrication for the alloy. The wear rate was observed to be significantly lower in lubricated contact compared to dry contact. As the applied load increases, the wear rate increases due to higher contact pressure, and as sliding speed increases, the wear rate also increases due to increased friction and heat generation. The obtained results showed that SLM-printed samples have a lower wear rate compared to the samples manufactured by the casting process. The type of lubricant affects the tribological behavior of the alloy, with gear oil providing the best results. Overall, the presented results can guide the selection of appropriate lubricants and operating conditions to minimize wear in Co-Cr-Mo alloy applications.

Author Contributions: Conceptualization, M.R. and Z.M.R.; methodology, M.R. and Z.M.R.; formal analysis, M.R.; investigation, M.R.; writing—original draft preparation, M.R.; writing—review and editing, M.R. and Z.M.R. All authors have read and agreed to the published version of the manuscript.

Funding: This research received no external funding.

Institutional Review Board Statement: Not applicable.

Informed Consent Statement: Not applicable.

Data Availability Statement: Data presented in this study are available upon request.

Conflicts of Interest: The authors declare no conflict of interest.

References

1. Song, C.; Zhang, M.; Yang, Y.; Wang, D.; Jia-kuo, Y. Morphology and properties of CoCrMo parts fabricated by selective laser melting. *Mater. Sci. Eng. A* **2018**, *713*, 206–213. [CrossRef]
2. Chen, Z.; Chen, A.; Jia, Q.; Xia, Z.; Li, R.; Wang, C.; Pan, J.; Shi, Y. Investigation of microstructures and strengthening mechanisms in an N-doped Co-Cr-Mo alloy fabricated by laser powder bed fusion. *Virtual Phys. Prototyp.* **2023**, *18*, e2219665. [CrossRef]
3. Liverani, E.; Fortunato, A.; Leardini, A.; Belvedere, C.; Siegler, S.; Ceschini, L.; Ascari, A. Fabrication of Co–Cr–Mo endoprosthetic ankle devices by means of Selective Laser Melting (SLM). *Mater. Des.* **2016**, *106*, 60–68. [CrossRef]
4. Lin, D.; Xi, X.; Li, X.; Hu, J.; Xu, L.; Han, Y.; Zhang, Y.; Zhao, L. High-temperature mechanical properties of FeCoCrNi high-entropy alloys fabricated via selective laser melting. *Mater. Sci. Eng. A* **2022**, *832*, 142354. [CrossRef]
5. Khimich, M.A.; Ibragimov, E.A.; Saprykina, N.A.; Sharkeev, Y.P.; Saprykin, A.A. Co-Cr-Mo alloy produced via powder bed laser fusion. *AIP Conf. Proc.* **2020**, *2310*, 20144.
6. Li, H.; Ramezani, M.; Chen, Z. Dry sliding wear performance and behaviour of powder bed fusion processed Ti–6Al–4V alloy. *Wear* **2019**, *440–441*, 203103. [CrossRef]
7. Knieps, M.S.; Messé, O.M.D.M.; Barriobero-Vila, P.; Hecht, U. Advanced characterization of two novel Fe-rich high entropy alloys developed for laser powder bed fusion in the Al-Co-Cr-Fe-Ni-Zr system. *Materialia* **2022**, *26*, 101615. [CrossRef]
8. da Silva Costa, A.M.; Oliveira, J.P.; Munhoz, A.L.J.; Leite, E.G.B.; de Freitas, D.S.; de Jesus Monteiro, M.; Rodriguez, J. Co–Cr–Mo alloy fabricated by laser powder bed fusion process: Grain structure, defect formation, and mechanical properties. *Int. J. Adv. Manuf. Technol.* **2021**, *116*, 2387–2399. [CrossRef]
9. Li, H.; Ramezani, M.; Chen, Z.; Singamneni, S. Effects of process parameters on temperature and stress distributions during selective laser melting of Ti-6Al-4V. *Trans. Indian Inst. Met.* **2019**, *72*, 3201–3214. [CrossRef]
10. Dong, X.; Li, N.; Yu, J.; Qu, Y.; Wu, M.; Zhou, Y.; Shi, H.; Peng, H.; Zhang, Y.; Yan, J. Effect of grain boundary character on isothermal phase transformation and mechanical properties of Co-Cr-Mo alloy fabricated by selective laser melting. *J. Alloys Compd.* **2022**, *903*, 163904. [CrossRef]

11. Tonelli, L.; Fortunato, A.; Ceschini, L. CoCr alloy processed by Selective Laser Melting (SLM): Effect of Laser Energy Density on microstructure, surface morphology, and hardness. *J. Manuf. Process.* **2020**, *52*, 106–119. [CrossRef]
12. Roudnicka, M.; Bigas, J.; Molnarova, O.; Palousek, D.; Vojtech, D. Different Response of Cast and 3D-Printed Co-Cr-Mo Alloy to Heat Treatment: A Thorough Microstructure Characterization. *Metals* **2021**, *11*, 687.
13. Takaichi, A.; Kajima, Y.; Kittikundecha, N.; Htat, H.L.; Wai Cho, H.H.; Hanawa, T.; Yoneyama, T.; Wakabayashi, N. Effect of heat treatment on the anisotropic microstructural and mechanical properties of Co–Cr–Mo alloys produced by selective laser melting. *J. Mech. Behav. Biomed. Mater.* **2020**, *102*, 103496. [CrossRef] [PubMed]
14. Wang, Z.; Tang, S.Y.; Scudino, S.; Ivanov, Y.P.; Qu, R.T.; Wang, D.; Yang, C.; Zhang, W.W.; Greer, A.L.; Eckert, J.; et al. Additive manufacturing of a martensitic Co–Cr–Mo alloy: Towards circumventing the strength–ductility trade-off. *Addit. Manuf.* **2021**, *37*, 101725. [CrossRef]
15. Roudnická, M.; Orsolya Molnárová, O.; Jan Drahokoupil, J.; Jiří Kubásek, J.; Jiří Bigas, J.; Vít Šreibr, V.; David Paloušek, D.; Dalibor Vojtěch, D. Microstructural instability of L-PBF Co-28Cr-6Mo alloy at elevated temperatures. *Add. Manuf.* **2021**, *44*, 102025. [CrossRef]
16. Schwindling, F.S.; Seubert, M.; Rues, S.; Koke, U.; Schmitter, M.; Stober, T. Two-body wear of CoCr fabricated by selective laser melting compared with different dental alloys. *Tribol. Lett.* **2015**, *60*, 25. [CrossRef]
17. Duran, K.; Mindivan, H.; Atapek, S.H.; Simov, M.; Dikova, T. Tribological characterization of cast and selective laser melted Co-Cr-Mo alloys under dry and wet conditions. In Proceedings of the 19th International Metallurgy & Materials Congress, Istanbul, Turkey, 25–27 October 2018.
18. Fu, W.; Liu, S.; Jiao, J.; Xie, Z.; Huang, X.; Lu, Y.; Liu, H.; Hu, S.; Zuo, E.; Kou, N.; et al. Wear resistance and biocompatibility of Co-Cr dental alloys fabricated with CAST and SLM techniques. *Materials* **2022**, *15*, 3263. [CrossRef]
19. Tonelli, L.; Ahmed, M.M.Z.; Ceschini, L. A novel heat treatment of the additively manufactured Co28Cr6Mo biomedical alloy and its effects on hardness, microstructure and sliding wear behavior. *Prog. Addit. Manuf.* **2022**, *8*, 313–329. [CrossRef]
20. *ASTM F75-23*; Standard Specification for Cobalt-28 Chromium-6 Molybdenum Alloy Castings and Casting Alloy for Surgical Implants (UNS R30075). ASTM International: West Conshohocken, PA, USA. Available online: https://www.astm.org/f0075-23.html (accessed on 30 July 2023).
21. Huang, Z.; Wang, B.; Liu, F.; Song, M.; Ni, S.; Liu, S. Microstructure evolution, martensite transformation and mechanical properties of heat treated Co-Cr-Mo-W alloys by selective laser melting. *Int. J. Refract. Met. Hard Mater.* **2023**, *113*, 106170. [CrossRef]
22. Li, H.; Chen, Z.; Ramezani, M. Wear behaviours of PVD-TiN coating on Ti-6Al-4V alloy processed by laser powder bed fusion or conventionally processed. *Int. J. Adv. Manuf. Technol.* **2021**, *113*, 1389–1399. [CrossRef]
23. Sing, S.L.; Huang, S.; Yeong, W.Y. Effect of solution heat treatment on microstructure and mechanical properties of laser powder bed fusion produced cobalt-28chromium-6molybdenum. *Mater. Sci. Eng. A* **2020**, *769*, 138511. [CrossRef]
24. Kim, K.-S.; Hwang, J.-W.; Lee, K.-A. Effect of building direction on the mechanical anisotropy of biocompatible Co–Cr–Mo alloy manufactured by selective laser melting process. *J. Alloys Compd.* **2020**, *834*, 155055. [CrossRef]
25. Ramezani, M.; Ripin, Z.M.; Ahmad, R. A static friction model for tube bulge forming using a solid bulging medium. *Int. J. Adv. Manuf. Tech.* **2009**, *43*, 238–247. [CrossRef]
26. Yang, X.; Li, C.; Ye, Z.; Zhang, X.; Zheng, M.; Gu, J.; Jiang, J. Effects of tribo-film on wear resistance of additive manufactured cobalt-based alloys during the sliding process. *Surf. Coat. Technol.* **2021**, *427*, 127784. [CrossRef]
27. Al-Aloosi, R.A.; Çomakli, O.; Yazici, M.; Taha, Z.A. Influence of Scanning Velocity on a CoCrMoW Alloy Built via Selective Laser Melting: Microstructure, Mechanical, and Tribological Properties. *J. Mater. Eng. Perform.* **2023**, *32*, 6717–6724. [CrossRef]
28. Li, H.; Chen, Z.; Ramezani, M. Effect of temperature on sliding wear behaviour of Ti-6Al-4V alloy processed by powder bed fusion additive manufacturing techniques. *J. Mater. Eng. Perform.* **2023**, *31*, 8940–8954. [CrossRef]